Biophysical Journal Volume 68 April 1995 1416–1422

Three-Dimensional Structure of Lipid Vesicles Embedded in Vitreous Ice and Investigated by Automated Electron Tomography

Karsten Dierksen,* Dieter Typke,* Reiner Hegerl,* Jochen Walz,* Erich Sackmann,‡ and Wolfgang Baumeister*
*Max-Planck-Institut für Biochemie, D 82152 Martinsried, and ‡Technische Hochschule München, D 82748 Garching, Germany

ABSTRACT Automated electron tomography is shown to be a suitable means to visualize the shape of phospholipid vesicles embedded in vitrified ice. With a slow-scan charge-coupled device camera as a recording device, the cumulative electron dose needed to record a data set of 60 projections at a magnification of 20,000× can be kept as low as 15 $e^-/Å^2$ (or 1500 electrons/nm^2). The membrane of the three-dimensionally reconstructed vesicles is clearly visible in two-dimensional sections through the three-dimensionally reconstructed volume. Some edges indicating a polygonal shape of the vesicles, frozen from the gel phase, are also clearly recognized. Because of the presently limited tilt angle range (±60°), the upper and lower "caps" of the vesicles (representing about 35% of the surface of the ellipsoidal particles) remain invisible in the three-dimensional reconstruction.

INTRODUCTION

Vesicles composed of lipid bilayers can be regarded, in some respects, as simple models of cell plasma membranes and intracellular organelles. Characteristic shape transitions (such as the discocyte-stomatocyte transition) or cellular events associated with shape instabilities (such as endocytosis) can be mimicked by simply varying the area-to-volume ratio of vesicles composed of a single lipid component (Käs and Sackmann, 1991; Lipowsky, 1991) or by changing the bilayer asymmetry (Käs and Sackmann, 1991).

Combined theoretical and experimental studies have shown that the rich manifold of shape changes of vesicles or cells may be described in terms of the minimum bending energy concept of soft shells subjected to the constraint of constant volume and membrane area (Helfrich, 1973; Lipowsky, 1992). In particular, the theory predicts that the shape changes do not depend on the size of the vesicles, at least at length scales that are large compared with the molecular dimensions.

Until now, shape changes induced by variation of the area-to-volume ratio or the coupling between curvature and phase separation have only been studied by light microscopy, which is restricted to giant vesicles of sizes larger than 5 μm. The transient shapes of small vesicles may be frozen-in by cryo-fixation and observed by transmission electron microscopy (Lepault et al., 1985; Frederik et al., 1989; Siegel et al., 1994). However, conventional cryomicroscopy provides only two-dimensional projections of the contours of vesicles. Important details such as the interconnection of small vesicles by narrow necks (caused by budding) can only be detected in rare cases when they are properly oriented and not overlapping each other. A true three-dimensional (3D) image will be of great advantage because it enables us to separate overlapping structures. In the present work, we demonstrate that automated electron tomography (AET), a technique that was recently developed in our laboratory (Typke et al., 1991; Dierksen et al., 1992, 1993), allows the reconstruction of the 3D shape of frozen hydrated vesicles to a high precision. One disadvantage encountered so far is that the limited tilt angle range prohibits the visualization of the upper and lower caps of the vesicles. This limitation will largely be overcome once cryo-holders allowing for tilt angles up to ±80° are available.

MATERIALS AND METHODS

Specimen preparation

Dipalmitoylphosphatidylcholine (DPPC, purity better than 99%) was purchased from Sigma Chemie (Deisenhofen, Germany). In aqueous suspension, DPPC bilayers exhibit two first-order phase transitions at 33°C ($L_{\beta'} \rightarrow P_{\beta'}$, smooth crystalline → crystalline ripple phase) and at 41°C ($P_{\beta'} \rightarrow L_{\alpha}$, crystalline ripple phase → liquid phase). Specimens of vesicles, embedded in vitreous ice, were prepared in the following way: About 1 ml of a 6–7 mM aqueous suspension of DPPC was sonicated at room temperature for 10 min using a Sonifier with microtip (model 250/450, Branson, Danbury, CT) to obtain small sized vesicles with diameters in the range of ~50–500 nm. To minimize artifacts due to evaporation, cryo-preparation was performed in an environmental chamber (Bellare et al., 1988) under controlled humidity (>98%) and temperature conditions; the temperature of 22°C used in our experiments is below both phase transition temperatures. A droplet of the vesicle suspension was applied to a 100×400 mesh grid covered with holey carbon film with pre-adsorbed gold clusters. After blotting the droplet, the grid was cryo-fixed by plunging into liquid ethane and transferred into liquid nitrogen.

Electron microscopy and image processing

For cryo-electron microscopy, a liquid nitrogen-cooled cryo-holder (Gatan, Pleasanton, CA) allowing for a tilt range of ±60° was used. Tilt series were recorded semi-automatically (i.e., with interactive checks of the lateral

Received for publication 26 September 1994 and in final form 13 January 1995.

Address reprint requests to Dr. Dieter Typke, Max-Planck-Institut für Biochemie, D-82152 Martinsried, Germany. Tel.: 49-89-8578-2632; Fax: 49-89-8578-82641; E-mail: typke@vms.biochem.mpg.de.

Dr. Dierksen's current address: Bayer AG, D-51368 Leverkusen, Germany.

Abbreviations used: 3D, three-dimensional; DPPC, dipalmitoylphosphatidylcholine; AET, automated electron tomography; TEM, transmission electron microscope; FEG, field emission gun; CCD, charge-coupled device; psf, point spread function.

0006-3495/95/04/1416/07 $2.00

alignment of the images) using a CM 20 FEG transmission electron microscope (Philips, Eindhoven, The Netherlands), equipped with a CH 220 slow-scan CCD camera with a 1024×1024 pixel chip (Photometrics, Tucson, AR) and a VIPS 1000 computer with VAP 80 array processor (TVIPS GmbH, Gauting, Germany). The charge-coupled device (CCD) camera is adapted to the microscope by a rotary flange, allowing one to orient one edge of the CCD chip parallel to the direction of the tilt axis in the image (for further details, see Principles and Procedures of Automated Electron Tomography). The accelerating voltage was 120 kV, the EM magnification was 20,000×, the defocus was about 7 μm, and the tilt angle ranged from −60° to +60° with 2° increments (61 projection images). Images were recorded with 2×2 binning of pixels during readout of the CCD camera, i.e., with 512×512 pixel images. Because the size of a single pixel of the CCD chip was 19 μm, and the postmagnification factor between the film plane of the microscope and the entrance screen of the camera was 1.92×, the pixel size at the specimen level is 1.0 nm for the chosen imaging conditions. The software for the automatic control of tomographic procedures was developed in our laboratory using the high-level command language TCL (Technical Command Language, Technical University Delft, The Netherlands).

Correlation-based lateral alignments of the projections and 3D reconstructions were carried out using the EM software package (Hegerl and Altbauer, 1982). As reconstruction algorithm, filtered back-projection was used.

PRINCIPLES AND PROCEDURES OF AUTOMATED ELECTRON TOMOGRAPHY

Automation of complex imaging procedures such as electron tomography has become feasible with the advent of microprocessor-controlled transmission electron microscopes, large-area slow-scan CCD cameras and fast computers suitable for on-line image processing. Automated electron tomography (AET) enables to record a set of images of a specimen at different projection angles, distributed over a large angular range, in an automatic or semi-automatic fashion. To a good approximation, a TEM image can be considered to be a two-dimensional projection of the specimen. From such a set of projections, usually termed a "tilt series", or 3D data set, the 3D structure of the specimen is calculated using specialized image processing software (such as the EM software package). Because a slow-scan CCD camera is used as recording device, the images are immediately available in digitized form. In combination with a fast computer, the camera also serves as an essential element in the computer control of tomographic procedures. Because of the limited resolution of the scintillator at the entrance of our CCD camera (a 15-μm-thick multicrystalline P20 screen), we normally use the camera with 2×2 binning of pixels, i.e., with 512×512 pixel images.

The control of a tomographic procedure involves four basic steps that have to be carried out repeatedly: 1) setting a new tilt angle, 2) measuring and correcting for lateral displacements, 3) measuring and correcting for focus changes (autofocus), and 4) recording an image of the 3D data set. For organic or biological specimens, data collection has to be carried out under low dose conditions.

The correction of lateral displacements is necessary for every tilt angle. This becomes obvious if one considers the fact that one edge of the image field of the CCD camera, considered with respect to the specimen plane (e.g., ~500 nm at 20,000× EM magnification), is much smaller than the mechanical inaccuracy of the tilt axis, which is better than about ±1 μm for a normal specimen holder, but about ±5 μm for our cryo-holder even for optimum alignment of the specimen to the eucentric height. Lateral displacements are "measured" by calculating the cross-correlation function between a new image and a reference image, recorded previously, and determining the position of the cross-correlation peak, from which the relative displacement between both images can be deduced. The displacement is then corrected using the electromagnetic image shift facility of the microscope. For this purpose, the CM 20 FEG is used in the SEARCH state of the TEM LOW DOSE mode, which provides the image shift facility in Cartesian coordinates with a sensitivity of about 0.8 nm/step. We require the displacement correction to be sufficiently accurate to keep about 90–95% of the specimen area of the 0°-projection throughout a tilt series; this means that it does not need to be extremely precise. It is possible, therefore, to use images recorded with very low dose and reduced resolution (e.g., recorded with 8×8 binning of pixels) for this purpose. This reduces the dose required for the lateral alignment considerably and allows us to record these images on the same specimen area as those of the 3D data set (the "exposure area"), thus somewhat deviating from strict low dose conditions (~30% additional dose).

Focus changes are much less critical; corrections may be done after several tilt angle steps. The defocus is measured by recording two images, with the primary beam tilted by several mrad in opposite directions (Koster and de Ruijter, 1988). The relative displacement of the images, measured again by cross-correlation, allows us to calculate the actual and to set the desired defocus (using appropriate calibrations). Because focusing is usually done on a specimen area that is displaced in tilt axis direction, it does not contribute to the dose applied to the exposure area.

Typically, a tilt series consisting of 61 projections can be recorded at 20,000× EM magnification using a cumulative electron dose of 1000–2000 electrons/nm^2. The cumulative dose can thus be kept small enough that the technique can be applied to ice-embedded specimens. However, the considerably larger lateral displacements of the cryo-holder, its tendency to drift after setting a new tilt angle (at least in a certain angular range), and also the usually very low contrast of ice-embedded specimens introduce additional difficulties. It turned out that the lateral alignment had to be carried out iteratively; at least two steps, the first at lower magnification, are necessary at every tilt angle for the measurement and correction of lateral displacements. The contrast required for cross-correlations can sufficiently be improved by previously adsorbing gold clusters on the holey carbon film used for specimen preparation.

RESULTS AND DISCUSSION

Recording of tilt series

Several tilt series were recorded from samples of DPPC vesicles in vitreous ice, prepared as described. Two of these

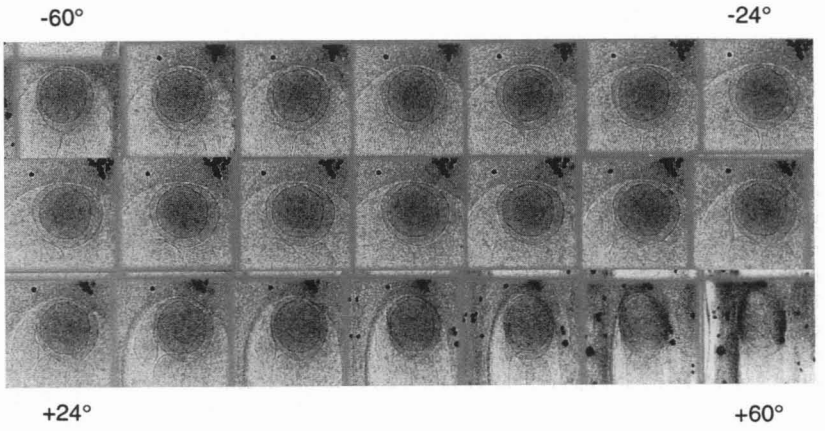

FIGURE 1 21 of the 61 projections, after lateral alignment, of a tilt series of DPPC vesicles in vitrified ice, prepared on holey carbon film. The carbon film carrying several gold clusters is visible in the upper part of the projections. The imaging conditions of the tilt series were $U = 120$ kV; $\Delta z = 7$ μm; $M_{EM} = 20{,}000\times$; 512^2 pixel images (recorded with 2×2 binning); (binned) pixel size 1 nm at specimen level; tilt angle range ± 60° with 2° increments; cumulative electron dose 1500 e^-/nm^2.

series have been evaluated. In the following, we present results of one series showing a specimen area that contains two vesicles enclosing each other. The vesicle surfaces of the second 3D reconstructed image look similar to those of the series shown here. The accelerating voltage of 120 kV used here was a compromise providing a good sensitivity of the scintillation screen of the CCD camera and sufficient penetration power for ice-embedded specimens of 100- to 200-nm thickness.

Lateral alignments during data recording were carried out at EM magnifications 3,800× and 20,000×. The log-file containing records of the alignment and refocusing steps and the mean image intensities tells us that the cumulative lateral shift corrections amount to ~7 μm, although the adjustment to the eucentric height was good, as judged from the small corrections necessary in the vicinity of zero tilt angle. Strong lateral displacements of ~500 nm for every 2° tilt angle step occurred between 6° and 20°. Displacements of this size can only be tracked at magnifications below 10,000×. The cumulative change of the defocus in the tilt series was ~3 μm. The cumulative mean image intensities of alignment and data recording steps correspond to a total dose of ~1500 e^-/nm^2. Of this dose, less than 2% was spent for pre-alignments and ~20% was spent for fine alignments. Focusing was carried out on a different specimen area and, thus, did not contribute to the dose delivered to the exposure area.

Fig. 1 shows 21 of the 61 projection images of this tilt series after lateral alignment. Although the contrast of the vesicle surfaces is low, partly due to the low dose used to record single projections, they can be recognized. One observes a cluster of small ice-embedded vesicles, situated close to the edge of a hole in the carbon film. Most clearly seen are the two vesicles enclosing each other. The carbon film, in the upper part of the projections, carries a number of gold clusters; these are useful not only to keep the correct specimen area in the field of view of the CCD camera, but also for the lateral alignment of the projections, the first and most important step in subsequent off-line image processing.

Alignment and 3D reconstruction

Several alignments were carried out using different subareas of the images and somewhat different conditions. Normally, the images are stretched perpendicular to the tilt axis by $1/\cos\alpha$ (α being the tilt angle), and then the relative shifts are determined sequentially by cross-correlation (Guckenberger, 1982). This procedure, which assumes a thin extended specimen, is problematic in this case, because 1) the specimen thickness is about 180 nm in its thickest parts, and 2) there is a pre-tilt of about 15° (which was determined during the course of the 3D reconstruction). The alignment obtained in this way, therefore, is relatively poor. The best result of the alignment was obtained by cutting out small areas around the single gold cluster in the upper left part of the images and correlating them, without stretching, with the corresponding area of the 0° projection.

It is interesting that the visibility of the membranes in the 3D reconstructed images does not depend much on the quality of the alignment (the quality being judged from the 3D reconstruction of gold clusters). The reason may be that only a few neighboring projections contribute to a specific part of the vesicles' surfaces, and for these projections the alignment may be good even if the total alignment is rather poor. Gold clusters, however, become strongly distorted for such an alignment. This is demonstrated in Fig. 2, *a* and *b*, which show *x-y*, *x-z*, and *y-z* sections through the center of the single gold cluster for the optimum (*a*) and the "normal" (*b*) alignments, respectively. (Note that in our convention the *y* axis is parallel to the tilt axis.) Even for the optimum alignment of the input projections, the reconstructed gold cluster exhibits distortions, which are typical for single-axis tilting with limited tilt angle range (i.e., missing data in the "missing cone," or better, for single-axis tilting, in the "missing wedge" of the reciprocal space): the image of the gold cluster is elongated in the *z*-direction, and there are strong side minima in the *x*-direction. These are effects of convoluting the ideal 3D image of the particle with the 3D point spread function for the chosen imaging and reconstruction conditions. In addition, a "bad" alignment produces an anisotropic pattern in the background, e.g., in the interior of the vesicles.

Although the alignment was calculated at full resolution, a first 3D reconstruction was carried out at reduced resolution (1:4, i.e., with 4-nm pixel size). Fig. 3 *a–c* display sets of

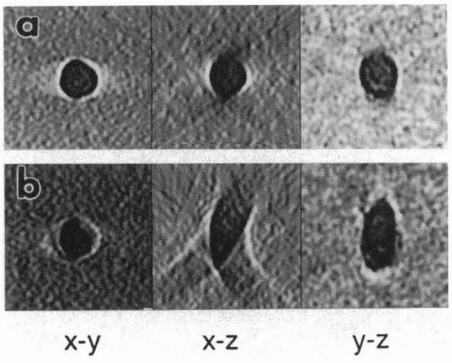

FIGURE 2 Central x-y, x-z and y-z sections, respectively, through the 3D image of a gold cluster, reconstructed at full resolution, (*a*) for optimum alignment of the projections, using only a small area around the gold cluster and no stretching, (*b*) for sequential (i.e., "normal") alignment of the projections, using large image areas. The distortion of the gold cluster in *a*, i.e., an elongation and ill defined surface in the z-direction, is caused by the limited tilt angle range of $\pm 60°$. In *b* although the alignment of neighboring projections is quite good, the progressive deviation from the correct alignment produces a strongly distorted image of the gold particle.

slices at 4-nm distances through the 3D reconstructed volume, parallel to the x-y, x-z, and y-z planes, respectively. Fig. 3 *d* is a schematic drawing showing the specimen geometry. In the sections, the membranes are seen much clearer than in single projections. They can be seen, however, only in a limited number of sections; the upper and lower caps remain invisible. This is even more obvious in the x-z sections: the membrane is visible only in those parts where a tangent plane to the surface has at least an angle of about 30° against the x-y plane. The invisibility of the (smooth) vesicle caps is again a limitation due to the limited tilt angle range and will be discussed in more detail below. It is possible, nevertheless, to recognize the surfaces of the ice film, including the upper and lower parts of the vesicle surfaces, due to some granular structures, which are presumably small ice granules. These are most clearly visible in the x-y sections (see *arrowheads* in Fig. 3 *a*). From the distribution of these structures, we infer that the thickness of the ice film outside the vesicles is between 80 nm (*lower left corner*) and 110 nm (*upper right corner*). The thickness of the vesicles in the center of the image field is about 180 nm. Because the granular structures get into contact with the surfaces of the outer vesicle in sections where the surface seems to disappear, it is also quite obvious that this vesicle extends to the ice surface. There may be a very thin ice layer, including the granules, on the upper and lower surfaces. Possibly, the inner vesicle also contacts the surfaces of the ice film; this, however, cannot be decided from the 3D reconstructed image. The lateral dimensions of the vesicles are 290 and 240 nm, respectively; thus, it is clear that they are somewhat compressed perpendicular to the ice film. This compression is most likely due to capillary forces exerted on the vesicles in the short (1–2 s) period of time between blotting of the excess fluid and plunge freezing. For the ellipsoid-shaped vesicles of dimensions given above, the invisible caps contain about 35% of the surface.

The absence of contrast in the caps can be understood from the following consideration: it is well known that the information about the density distribution across a layer oriented parallel to the x-y plane is confined to the z^* axis in reciprocal space. We may assume that the density distribution of lipid bilayers within the plane of the layer will not be resolved for the chosen imaging conditions. In a single-axis tilt series with tilt angles up to α_{max}, no data are recorded along the z^* axis or along other central lines within the "missing wedge." This means that (smooth) layers with an arbitrary density distribution across the layer will be totally invisible in the 3D reconstruction if their normals point into the corresponding wedge in real space (e.g., up to $90° - \alpha_{max}$ against the x-y plane for tilts about the y axis, or up to 90° for tilts about the x axis).

This result seems to be paradoxical in view of the fact that the 3D point spread function (psf) corresponding to such a data set is elongated only by a factor 1.4 in the z-direction (compared with the x- and y-directions). However, one has to take into account that the psf oscillates in the x-direction, exhibiting strong minima and maxima (see, e.g., Hoppe and Hegerl, 1982). Consequently, the convolution of the psf with any plane, the normal to which points into a direction corresponding to the missing wedge in reciprocal space, will be zero. It is thus reasonable that we are unable to visualize the vesicle caps.

The most promising way to improve the situation is a further extension of the tilt angle range, e.g., to $\pm 80°$. This will largely reduce, but not fully eliminate, the problem. Another way out of the limitation may be the use of constraints to improve the result of the 3D reconstruction (Barth et al., 1989; Sezan, 1992).

Fig. 4 displays a central x-y section through the 3D image of the tilt series, reconstructed at full resolution (i.e., 1-nm pixel size) with a frequency cutoff at $(5\ \text{nm})^{-1}$. Note that for 7-μm underfocus and 120-kV accelerating voltage, the phase contrast transfer function has its first zero at a spatial frequency of $(4.8\ \text{nm})^{-1}$. Information beyond this limit will certainly be transferred into the images, however, changing the sign of the contrast transfer function. For visibility of the membranes, no resolution better than 5 nm is required. Another consideration concerns the resolution limitation due to the finite angular increment of 2° (or $\Delta\alpha = 3.5$ mrad). Because the specimen thickness is ~180 nm, we may estimate the resolution for a cylinder of this diameter. For the full 180° tilt range, the isotropic resolution (see, e.g., Hoppe and Hegerl, 1982) would be $d = \Delta\alpha \cdot D = 6.3$ nm, where D is the diameter. The limited tilt range ($\pm 60°$) does not much affect the resolution in the x-y plane, but it produces the aforementioned elongation of the psf in the z-direction and strong side minima in the x-direction. The conditions

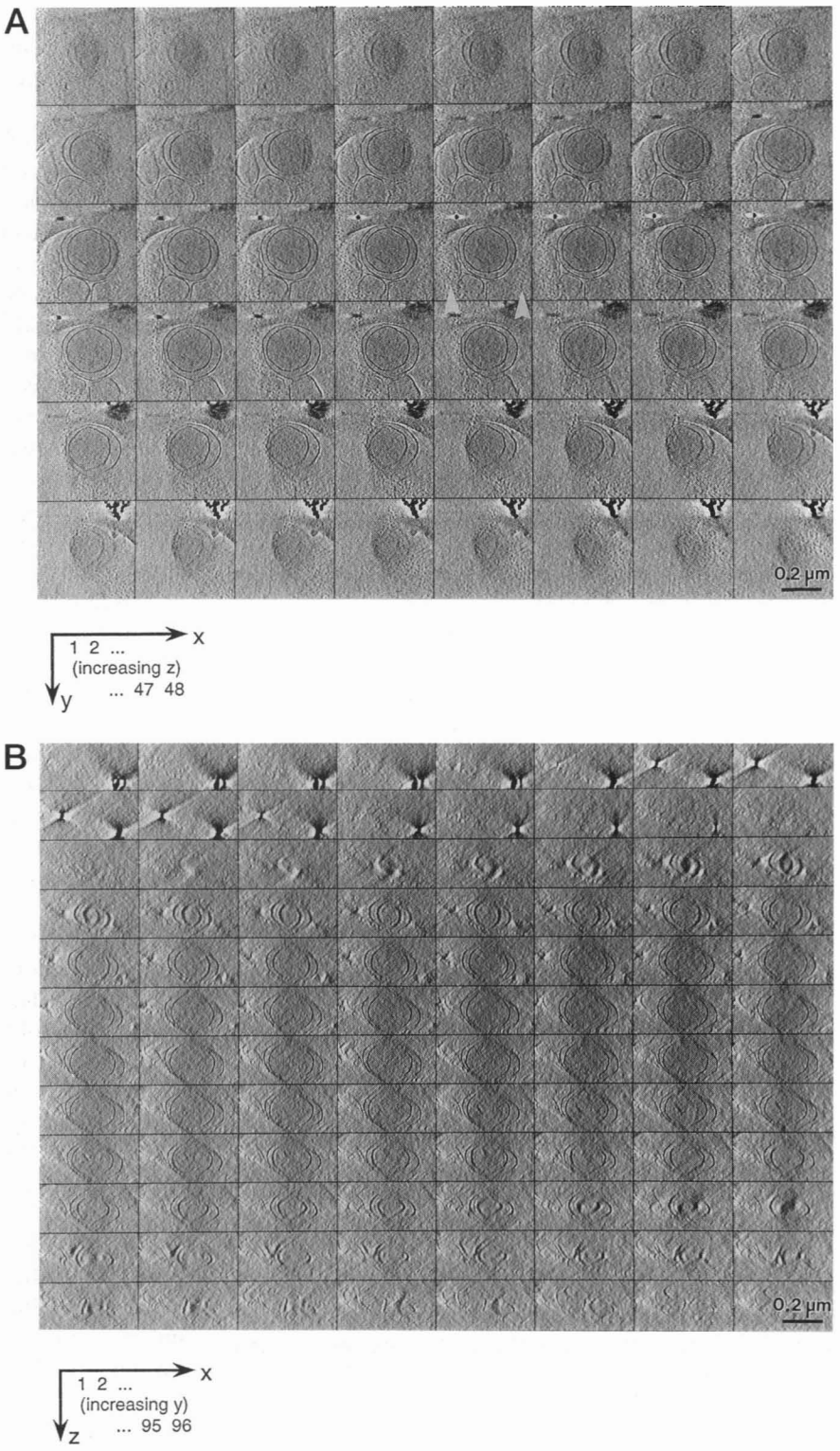

FIGURE 3 Sets of slices at 4-nm distances through the 3D reconstructed volume (reconstructed at reduced (1.4) resolution); (*a*) *x-y* slices (128×128 pixels, pixel size 4 nm). The membrane is clearly visible in the slices. In several slices, edges of the vesicles can be recognized, indicating their tendency to assume a polygonal shape. Arrowheads point to granular structures that seem to be present on both surfaces of the ice film. (*b*) Set of *x-z* slices (128×64 pixels). (*c*) Set of *y-z* slices (128×64 pixels). (*d*) Scheme of the reconstructed volume (*x-z* section).

when recording this tilt series (defocus and tilt angle increment) thus were just adequate to visualize the membrane as a whole. Because of the limited resolution, the membranes seem to have a thickness of ~6 nm in the *x-y* section shown in Fig. 4; this is somewhat more than expected from the length of the tails of DPPC molecules.

The double-layer structure of the membrane can be visualized in projection at a defocus of ~1–2 μm. However, to resolve the bilayer in a 3D image of the present specimen, a 1° tilt angle increment and possibly a somewhat higher magnification would be required.

Visualization of defects

A closer inspection of the *x-y* sections (Fig. 3 *a*) shows that the vesicles exhibit a slightly polygonal shape. The edges and

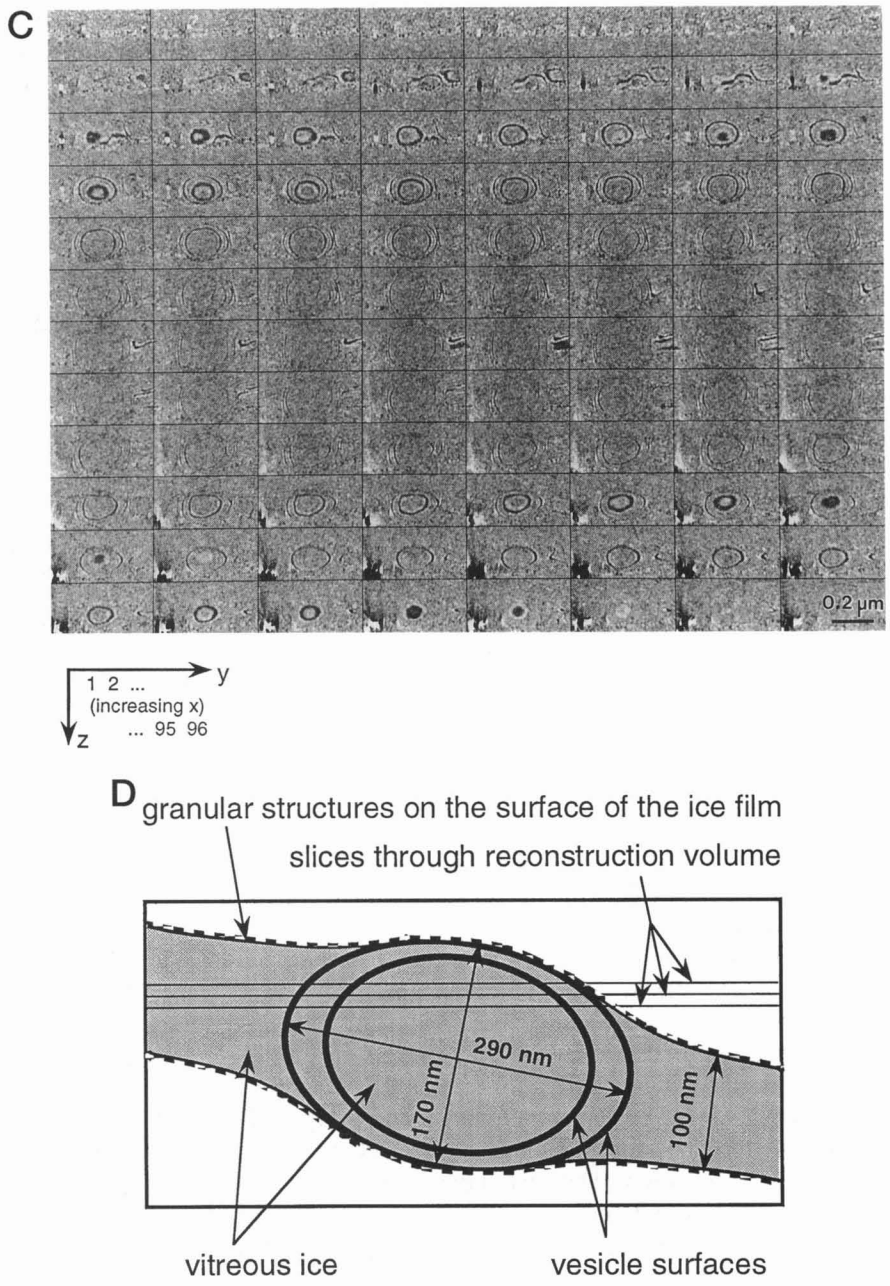

FIGURE 3 *Continued*

the tendency to assume a polygonal shape are expected for the following reasons. Because the bending stiffness of bilayers in the $L_{\beta'}$ phase is very high, they tend to be flat. Therefore, the vesicle shells are composed of flat pieces. As is well known from freeze-fracture studies, two adjacent flat pieces meet along wall defects. Two types of wall defects have been found (Rüppel and Sackmann, 1983): 1) Neél-walls and 2) breaks. The former arise along lines where two regions with opposite directions of chain tilting meet; the latter arise because of mutual shifting of the bilayers in the direction of the bilayer normal. Neél-wall defects produce edges (and corners at points where several Neél walls meet), and breaks facilitate the build-up of curved vesicles from flat crystalline slices of bilayers.

Concluding remarks

It has been demonstrated that AET is a suitable means to visualize the three-dimensional shapes of ice-embedded vesicles, however, because of the presently limited tilt angle range of ±60°, about one-third of the surface remains invisible in the 3D reconstructed image. The automation of tomographic low dose procedures clearly has a number of advantages: first, it relieves the operator of performing manually all of the intermediate steps between two exposures, which are necessary in recording low dose tilt series. Consequently, there is no practical limitation to the number of projections; the number of projections is in fact limited by the requirement that the dose has to be high enough to allow the lateral alignment

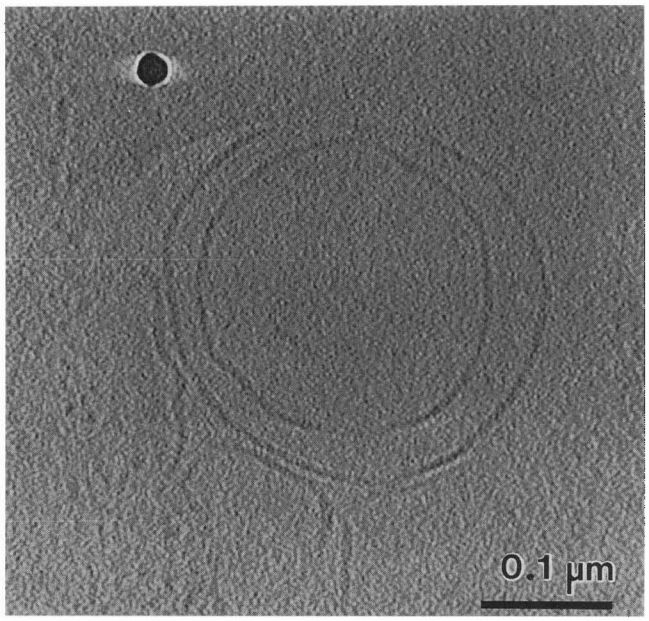

FIGURE 4 Central x-y section through the 3D reconstructed volume at full resolution, with frequency cutoff at $(5\ \text{nm})^{-1}$.

of the projections by means of cross-correlation (Dierksen et al., 1992). This, however, also depends on the specimen and can be manipulated to some extent, e.g., by the addition of strong contrast particles. The CCD camera delivers the images immediately in a digital format, and it makes it possible to record single images with a very low dose.

The time required to record a tilt series of 60 projections at intermediate magnifications (20,000×–40,000×) is about 1–2 h; the subsequent alignment and (a first) 3D reconstruction (at reduced resolution) takes about 2 h on a modern workstation. The technique is thus suited to study the shapes and shape variations of ensembles of vesicles, e.g., after fast-freezing from different starting temperatures. Because of the fluctuations in the parameters determining the shape of single vesicles, such a study will require a statistical evaluation of vesicle shapes, which means that many vesicles have to be analyzed. This will certainly be feasible, because a lower magnification would be sufficient (e.g., smaller by a factor of four compared with the tilt series evaluated above). Together with an improved resolution of the scintillation screen of the CCD camera due to a smaller thickness of the P20 scintillator, allowing one to record 1024^2 pixel images, a factor of 64 will be gained in the specimen area covered in a single tilt series. Thus, it will be possible to record for this kind of analysis data of many vesicles in a reasonable number of tilt series experiments.

We thank Dr. R. M. Glaeser for helpful discussions and critical reading of the manuscript.

REFERENCES

Barth, M., R. K. Bryan, and R. Hegerl. 1989. Approximation of missing-cone data in 3D electron microscopy. *Ultramicroscopy.* 31: 365–378.

Bellare, J. R., H. T. Davis, L. E. Scriven, and Y. Talmon. 1988. Controlled-environment vitrification system: an improved sample preparation technique. *J. Electron Microsc. Tech.* 10:87–111.

Dierksen, K., D. Typke, R. Hegerl, and W. Baumeister. 1993. Toward automatic electron tomography. II. Implementation of autofocus and low-dose procedures. *Ultramicroscopy.* 49:109–120.

Dierksen, K., D. Typke, R. Hegerl, A. J. Koster, and W. Baumeister. 1992. Toward automatic electron tomography. *Ultramicroscopy.* 40: 71–87.

Frederik, P. M., W. J. Green, and Y. Talmon. 1989. Phospholipid, nature's own slide and cover slip for cryo-electron microscopy. *J. Microsc.* 153: 81–92.

Guckenberger, R. 1982. Determination of a common origin in the micrographs of tilt series in three-dimensional electron microscopy. *Ultramicroscopy.* 9:167–174.

Hegerl, R., and A. Altbauer. 1982. The "EM" program system. *Ultramicroscopy.* 9:109–115.

Helfrich, W. 1973. Elastic properties of lipid bilayers. *Z. Naturforsch.* 28C: 693–703.

Hoppe, W., and R. Hegerl. 1982. Three-dimensional structure determination by electron microscopy (nonperiodic specimens). *In* Computer Processing of Electron Microscope Images. P. W. Hawkes, editor. Springer-Verlag, Berlin. 127–185.

Käs, J., and E. Sackmann. 1991. Shape changes and shape stability of giant phospholipid vesicles in pure water induced by area to volume changes. *Biophys. J.* 60:825–844.

Koster, A. J., and W. J. de Ruijter. 1992. Practical autoalignment of transmission electron microscopes. *Ultramicroscopy.* 40:89–107.

Lepault, J., F. Pattus, and N. Martin. 1985. Cryo-electron microscopy of artificial biological membranes. *Biochim. Biophys. Acta.* 820: 1315–1318.

Lipowsky, R. 1991. The conformation of membranes. *Nature.* 349:475–481.

Lipowsky, R. 1992. Budding of membranes induced by intramembrane domains. *J. Physique II.* 2:1825–1840.

Rüppel, D., and E. Sackmann. 1983. On defects in different phases of lipid bilayers. *J. Physique II.* 44:1025–1034.

Sezan, M. I. 1992. An overview of convex projections theory and its application to image recovery problems. *Ultramicroscopy.* 40:55–67.

Siegel, D. P., W. J. Green, and Y. Talmon. 1994. The mechanisms of lamellar-to-inverted hexagonal phase transitions: a study using temperature-jump cryo-electron microscopy. *Biophys. J.* 66:402–414.

Typke, D., K. Dierksen, and W. Baumeister. 1991. Automatic electron tomography. *Proc. 49th Annual Meeting EMSA*, San Jose. 544–545.